Electronic Supplementary Material (ESI) for Physical Chemistry Chemical Physics.

Supporting Information to

Thermodynamic versus Non-Equilibrium Stability of Palmitic Acid Monolayers in Calcium-Enriched Sea Spray Aerosol Proxy Systems

Bethany A. Wellen Rudd, Andrew S. Vidalis, and Heather C. Allen

Department of Chemistry & Biochemistry, The Ohio State University, Columbus, Ohio 43210, United States.

Determination of Tilt Angle with VSFG

The intensity of the measured SFG beam is proportional to the square of the second-order nonlinear susceptibility ($\chi^{(2)}_{eff}$), and is dependent on the polarization combination and experimental geometry of the three beams (SFG, visible, IR). $\chi^{(2)}_{eff}$ for the *ssp* and *ppp* polarization combinations are shown in eqn. (S1)-(S3), where L_{ii} are the nonlinear Fresnel factors,[1,2] and θ_i is the angle, relative to surface normal, of the incoming (visible, IR) and outgoing (SFG) beams.

$$I_{SFG} \propto \left|\chi^{(2)}_{eff}\right|^2 I_{vis} I_{IR} \tag{S1}$$

$$\chi^{(2)}_{eff,\,ssp} = L_{yy}(\omega_{SFG}) L_{yy}(\omega_{vis}) L_{zz}(\omega_{IR}) \sin\beta_{IR} \chi^{(2)}_{yyz}. \tag{S2}$$

$$\begin{aligned}\chi^{(2)}_{eff,\,ppp} = & - L_{xx}(\omega_{SFG}) L_{xx}(\omega_{vis}) L_{zz}(\omega_{IR}) \cos\beta_{SFG} \cos\beta_{vis} \sin\beta_{IR} \chi^{(2)}_{xxz} \\ & - L_{xx}(\omega_{SFG}) L_{zz}(\omega_{vis}) L_{xx}(\omega_{IR}) \cos\beta_{SFG} \sin\beta_{vis} \cos\beta_{IR} \chi^{(2)}_{xzx} \\ & + L_{zz}(\omega_{SFG}) L_{xx}(\omega_{vis}) L_{xx}(\omega_{IR}) \sin\beta_{SFG} \cos\beta_{vis} \cos\beta_{IR} \chi^{(2)}_{zxx} \\ & + L_{zz}(\omega_{SFG}) L_{zz}(\omega_{vis}) L_{zz}(\omega_{IR}) \sin\beta_{SFG} \sin\beta_{vis} \sin\beta_{IR} \chi^{(2)}_{zzz}\end{aligned} \tag{S3}$$

The orientation of the terminal methyl group (θ_{CH3}), with C_{3v} point group symmetry, is calculated from the symmetric and asymmetric stretches of the CH_3 mode in the *ssp* and *ppp* polarizations, respectively. The relevant $\chi^{(2)}_{ijk}$ elements used for the analysis are

$$\chi^{(2)}_{yyz,ss} = \frac{1}{2}N_s\beta_{ccc}\left[(1+R)\langle\cos\theta_{CH3}\rangle - (1-R)\langle cos^3\theta_{CH3}\rangle\right] \tag{S4}$$

$$\chi^{(2)}_{yyz,as} = \chi^{(2)}_{xxz,as} = -N_s\beta_{aca}\left[\langle\cos\theta_{CH3}\rangle - \langle cos^3\theta_{CH3}\rangle\right] \tag{S5a}$$

$$\chi^{(2)}_{yzy,as} = \chi^{(2)}_{xzx,as} = \chi^{(2)}_{zxx,as} = \chi^{(2)}_{zyy,as} = N_s\beta_{aca}\langle cos^3\theta_{CH3}\rangle \tag{S5b}$$

$$\chi^{(2)}_{zzz,as} = 2N_s\beta_{aca}\left[\langle\cos\theta_{CH3}\rangle - \langle cos^3\theta_{CH3}\rangle\right] \tag{S5c}$$

where *R*, in eqn. (S4), is the hyperpolarizability ratio defined as β_{aac}/β_{ccc} and is set as 2.3,[3] and the ratio of $\beta_{aca}/\beta_{aac} = 4.2$.[4] Assuming a δ-distribution for θ_{CH3}, the methyl group orientation can be found from the ratio of the $\chi^{(2)}_{ppp,as}$ to $\chi^{(2)}_{ssp,\,ss}$ elements.

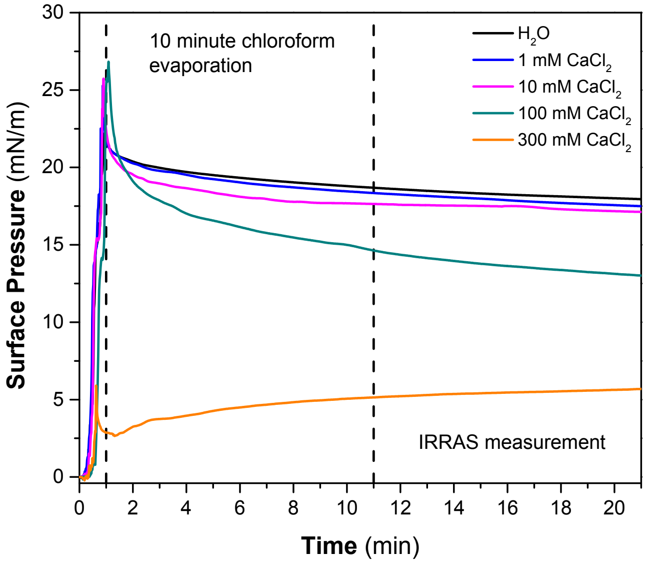

Fig. S1. Time evolution of surface pressure representative of an IRRAS measurement. d_{31}-PA monolayers are spread to 20.5 Å^2/molecule then 10 minutes are allowed for chloroform evaporation. These experiments show that surface pressure remains constant during the time period for an IRRAS measurements.

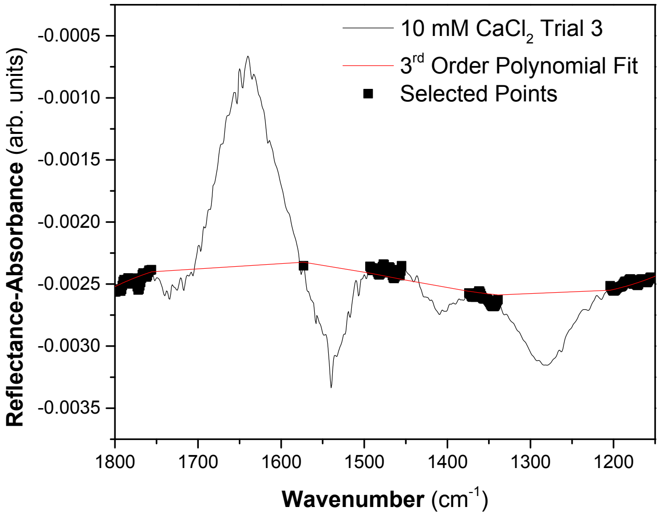

Fig. S2. Example of third-order polynomial baseline for IRRAS data in the headgroup region.

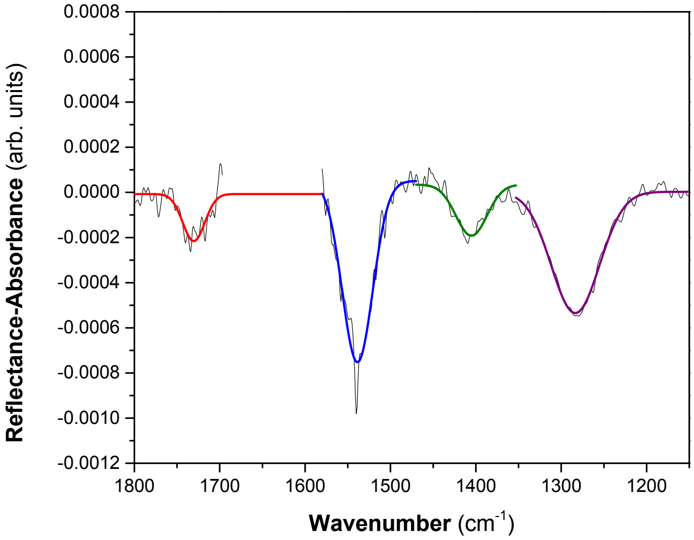

Fig. S3. Example of Gaussian fits of the headgroup modes of d_{31}-PA on a 10 mM $CaCl_2$ subphase. The water bending mode at ~1650 cm^{-1} is removed prior to the fit. Individual Gaussian functions are fit to each mode separately.

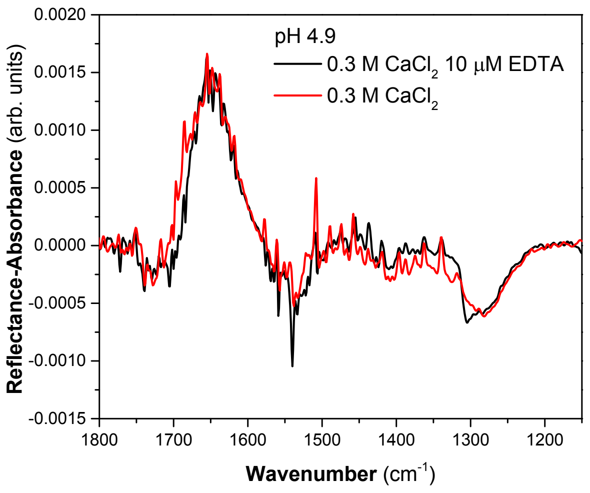

Fig. S4. IRRAS spectra of d$_{31}$-PA with and without EDTA on 0.3 M CaCl$_2$ solutions. The addition of 10 μM EDTA lowers the pH to 4.9, so a comparable 0.3 M CaCl$_2$ solution without EDTA was prepared at the same pH. As the spectra with and without EDTA are comparable, it is assumed that trace metals are not inducing the deprotonation of the PA monolayers. Because of the change in pH, the extent of deprotonation is not the same as the 0.3 M CaCl$_2$ spectrum presented in Fig. 1b.

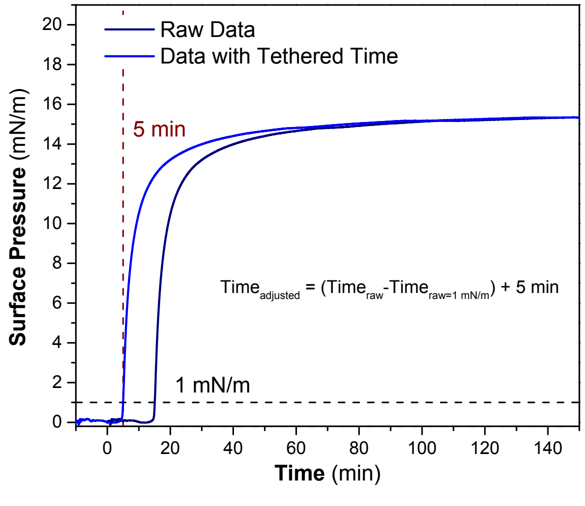

Fig. S5. Example of the time adjustment carried out for the ESP measurements for consistency in the curves. This trial is for a 1 mM CaCl$_2$ subphase. The time required to cause a rise in surface pressure above 0 mN/m from spontaneous monolayer formation via crystal elution is not significant and varies between trials. We have adjusted for this time so that ESP curves may be averaged and can be viewed on the same time scale. Curves are tethered such that a surface pressure of 1 mN/m corresponds to a time of 5 minutes (as shown by the equation in the figure). The value of the time adjustment for individual trials ranged from 5 to 50 minutes.

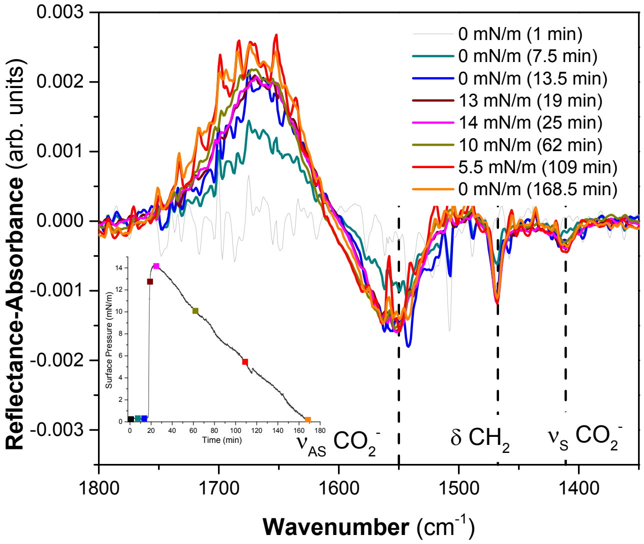

Fig. S6. IRRAS spectra of the headgroup region of PA monolayers on 300 mM $CaCl_2$ during the course of an ESP experiment. Deprotonation via Ca^{2+} binding of the PA molecules in the monolayer is immediately evident from the ν_{AS} and ν_S CO_2^- modes and remains unchanged during the course of the experiment.

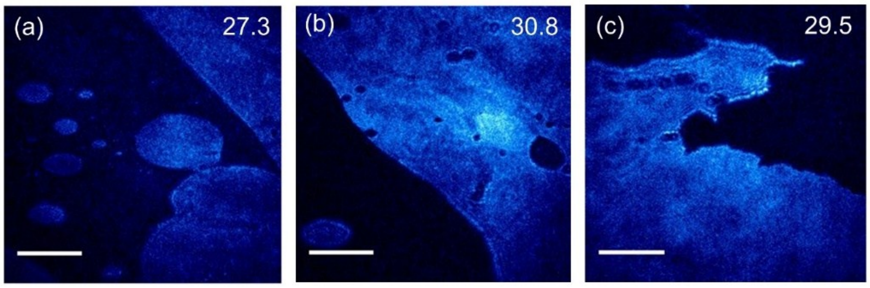

Fig. S7. BAM images of PA monolayers on (a) water, (b) 1 mM Cacl$_2$, and (c) 300 mM CaCl$_2$ in the gas-liquid condensed phase at 0 mN/m. The numbers in the upper right hand corner are the mean molecular areas of the systems when the image was captured. All scale bars represent 100 μm. These images demonstrated that even when the surface pressure of a system is 0 mN/m, there still exists a 2D monolayer presence, even though that monolayer may not be complete. The CaCl$_2$ subphases organize PA into large condensed sheets.

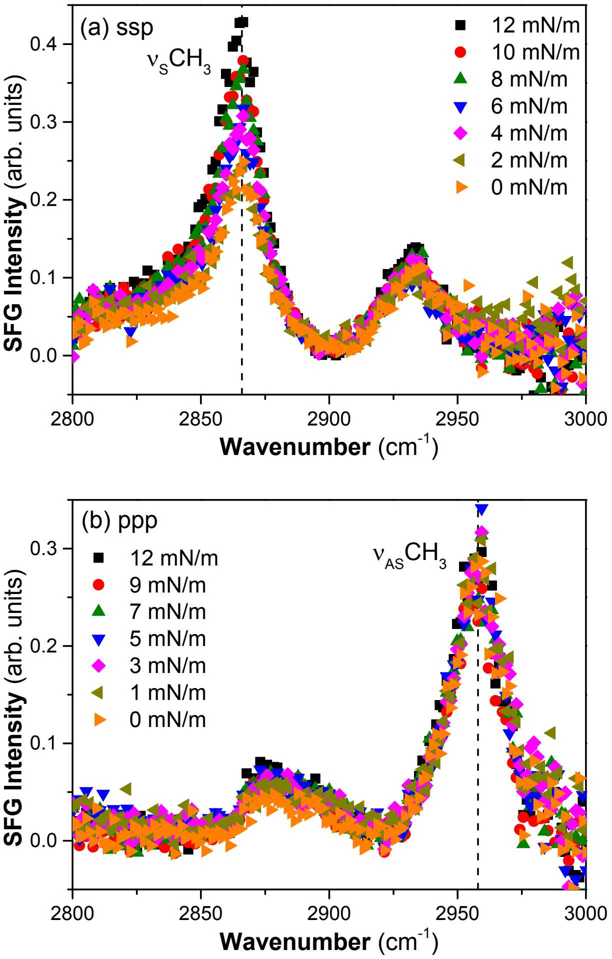

Fig. S8. VSFG spectra of PA in the CH stretching region tracking the surface pressure decline during an ESP measurement on 300 mM $CaCl_2$. The ratio of the ν_{AS} CH_3 (shown in (b)) in the *ppp* to the ν_S CH_3 (shown in (a)) in *ssp* can be used to determine the orientation of the methyl group which leads to the determination of the tilt angle.

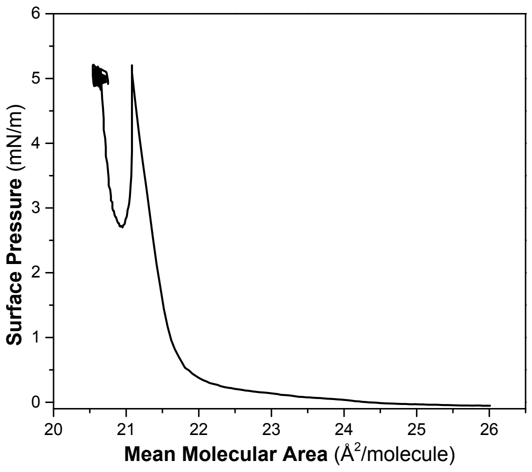

Fig. S9. Monolayer of PA on 300 mM $CaCl_2$ compressed to a target surface pressure of 5 mN/m. Upon reaching the target surface pressure, the barriers slow from a rate of 5 mm/min/barrier to a rate of 1 mm/min/barrier. This system exhibits a significant drop in surface pressure after reaching the target. The initial 2% drop in relative area is due to reestablishing the 5 mN/m surface pressure.

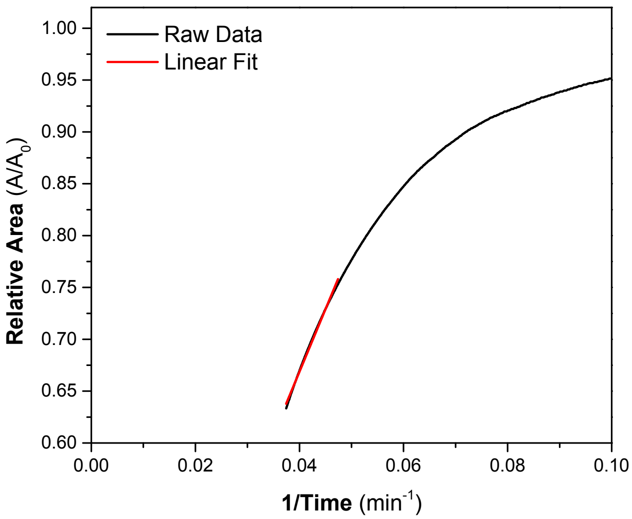

Fig. S10. Relative area plotted against the reciprocal of time (1/time) to determine A_∞. The y-intercept of the linear fit represents A_∞/A_0. Because A_0 is known, A_∞ can be calculated from the y-intercept.

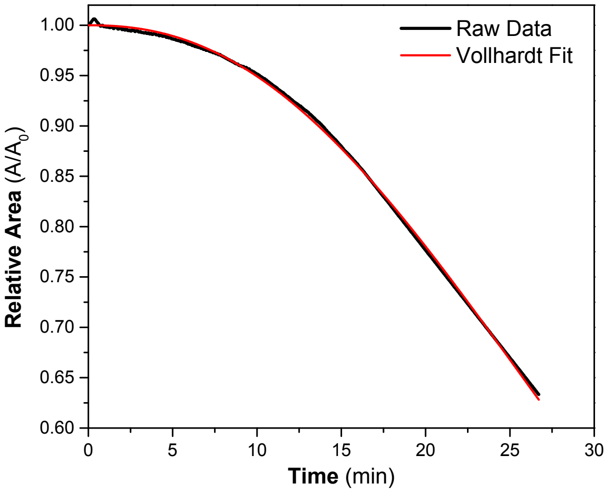

Fig. S11. PA relaxation data on water fit to the Vollhardt model at a constant surface pressure of 25 mN/m. In order to fit A/A_0 as the y axis, the Vollhardt function (eqn. (3)) was expanded and rearranged to the following form.

$$\frac{A}{A_0} = \left(1 - \frac{A_0 - A_\infty}{A_0}\right) + \left(\frac{A_0 - A_\infty}{A_0}\right) e^{-K_x t^x} \tag{S6}$$

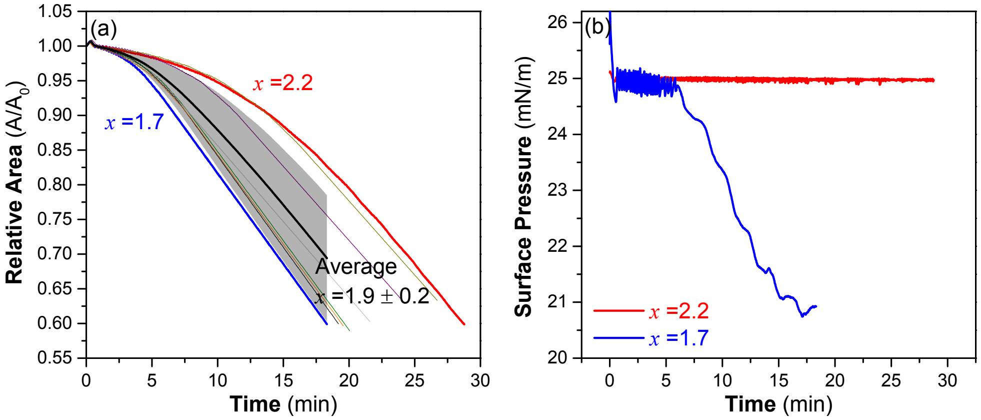

Fig. S12. Variability in constant pressure relaxation of PA on water at 25 mN/m (a). The ability of the system to maintain a 25 mN/m surface pressure affects the relative area vs. time curve, and thus the characteristic parameter, *x*.

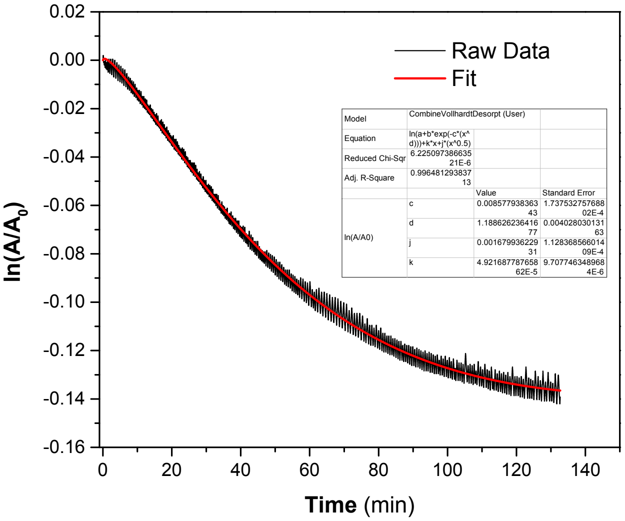

Model	CombineVollhardtDesorpt (User)		
Equation	ln(a+b*exp(-c*(x^d)))+k*x+j*(x^0.5)		
Reduced Chi-Sqr	6.22509738663521E-6		
Adj. R-Square	0.99648129383713		
		Value	Standard Error
ln(A/A0)	c	0.00857793836343	1.73753275768802E-4
	d	1.18862623641677	0.00402803013163
	j	0.00167993622931	1.12836856601409E-4
	k	4.92168778765862E-5	9.7077463489684E-6

Fig. S13. Example of the fit of PA relaxation on 1 mM $CaCl_2$ at 25 mN/m to eqn. (5).

References

1. R. R. Feng, Y. Guo, R. Lu, L. Velarde, H. F. Wang, *J. Phys. Chem. A*, 2011, **115**, 6015-6027.
2. H. F. Wang, W. Gan, R. Lu, Y. Rao, B. H. Wu, *Int. Rev. Phys. Chem.*, 2005, **24**, 191-256.
3. D. Zhang, J. Gutow, K. B. Eisenthal, *J. Phys. Chem.*, 1994, **98**, 13729-13734.
4. N. Watanabe, H. Yamamoto, A. Wada, K. Domen, C. Hirose, T. Ohtake, N. Mino, *Spectrochim. Acta, Part A*, 1994, **50**, 1529-1537.